PCCP

ROYAL SOCIETY OF CHEMISTRY

PAPER

View Article Online
View Journal | View Issue

Check for updates

Cite this: *Phys. Chem. Chem. Phys.*, 2023, **25**, 11684

Imaging the photodissociation dynamics of internally excited ethyl radicals from high Rydberg states

Luis Rubio-Lago,[a] David V. Chicharro,[a] Sonia Marggi Poullain,[a] Alexandre Zanchet,[b] Greta Koumarianou,†[c] Pavle Glodic,[c] Peter C. Samartzis,[c] Alberto García-Vela[b] and Luis Bañares *[ad]

Received 29th October 2022,
Accepted 17th March 2023

DOI: 10.1039/d2cp05082j

rsc.li/pccp

The site-specific hydrogen-atom elimination mechanism previously reported for photoexcited ethyl radicals (CH_3CH_2) [D. V. Chicharro *et al.*, *Chem. Sci.*, 2019, **10**, 6494] is interrogated in the photodissociation of the ethyl isotopologues CD_3CD_2, CH_3CD_2 and CD_3CH_2 through the velocity map imaging (VMI) detection of the produced hydrogen- and deuterium-atoms. The radicals, generated *in situ* from photolysis of a precursor using the same laser pulse employed in their excitation to Rydberg states, decompose along the C_α-H/D and C_β-H/D reaction coordinates through coexisting statistical and site-specific mechanisms. The experiments are carried out at two excitation wavelengths, 201 and 193 nm. The comparison between both sets of results provides accurate information regarding the primary role in the site-specific mechanism of the radical internal reservoir. Importantly, at 193 nm excitation, higher energy dissociation channels (not observed at 201 nm) producing low-recoil H/D-atoms become accessible. High-level *ab initio* calculations of potential energy curves and the corresponding non-adiabatic interactions allow us to rationalize the experimental results in terms of competitive non-adiabatic decomposition paths. Finally, the adiabatic behavior of the conical intersections in the face of several vibrational modes – the so-called vibrational promoting modes – is discussed.

1. Introduction

The photodissociation dynamics of the methyl radicals were studied by our group and published in 2016[1–3] as a first step of a wider project centered in the characterization of the photodissociation dynamics of small alkyl radicals using nanosecond pulsed laser excitation and velocity map or slice ion imaging detection.[4–8]

The reported translational energy and angular distributions of the H(^{2}S) photofragments produced in the photodissociation of the methyl radical from the 3s and 3p$_z$ Rydberg states highlighted different dissociation mechanisms.[2] A fast predissociation mechanism, characterized by the coupling between the 3s Rydberg state and a valence repulsive state, rationalizes the observed narrow translational energy distribution for photodissociation *via* the 3s Rydberg state. In contrast, the photodissociation on the 3p$_z$ Rydberg state, while initiated by a similar predissociation process through the coupling between the 3p$_z$ and a valence repulsive state, is constrained, later on, by two conical intersections that allow the system to relax to lower electronic states.

The photodissociation of the ethyl radical[9–20] was the natural second step in our quest. Our reference was the work of Fischer and co-workers, who had studied the 3s dissociation of the second simplest alkyl radical.[15] The bimodal energy distribution for the H-atoms obtained by Fischer and his group upon irradiation at 250 nm (3s Rydberg state) challenged the previous ethyl photodissociation model reported by Zhang and co-workers[14] grounded on a conical intersection between the pumped 3s Rydberg state and the ground state. Fischer and co-workers' proposal involved instead two different competitive pathways. A fast dissociation mechanism through a dissociative state yielding anisotropically distributed H-atoms gave rise to

[a] *Departamento de Química Física (Unidad Asociada I+D+i al CSIC), Facultad de Ciencias Químicas, Universidad Complutense de Madrid, 28040 Madrid, Spain. E-mail: lbanares@ucm.es*
[b] *Instituto de Física Fundamental, Consejo Superior de Investigaciones Científicas, C/Serrano, 123, 28006 Madrid, Spain*
[c] *Institute of Electronic Structure and Laser, Foundation for Research and Technology-Hellas (FORTH-IESL), Vassilika Vouton, 70013 Heraklion, Greece*
[d] *Instituto Madrileño de Estudios Avanzados en Nanociencia (IMDEA-Nanoscience), Cantoblanco, 28049 Madrid, Spain*
† Current address: Chemistry and Biochemistry Department, University of California Santa Barbara, Santa Barbara, CA 93106, USA.

the Gaussian-type structure peaking at higher translational energies. In contrast, a slow non-radiative decay generating low energetic H-atoms with isotropic angular distribution explained the Boltzmann-type contribution at low translational energies. Interestingly, the explanation provided by Fischer *et al.* required an active role of a valence state and a conical intersection in the photodissociation.

As indicated above, in earlier time, Zhang and co-workers carried out similar experiments at a slightly different excitation wavelength (245 nm).[14] While a qualitatively similar bimodal distribution was obtained by Zhang and co-workers, the branching ratio between the fast and the slow contributions was significantly larger. In addition, the average translational energy, $\langle E_t \rangle$, for the fast contribution obtained by Zhang and co-workers ($\langle E_t \rangle \sim 2.6$ eV), was considerably larger than the one obtained later on by the Fischer group ($\langle E_t \rangle \sim 1.8$ eV). In other words, the fast H-atoms observed by the Zhang group were much faster than those observed by the Fischer group. We thought that the reasons behind such differences could indeed be attributed to the different radical production and fragment detection techniques employed in both experiments. Fischer and co-workers generated ethyl radicals by flash pyrolysis of a precursor molecule right at the supersonic expansion of the molecular beam, while Zhang and co-workers used 193 nm photolysis of a precursor instead. Although the implication of the radical generation method on the photodissociation dynamics of the radical was not known at the time, we kept the issue in mind. On the other hand, we thought that the H-atom Rydberg tagging technique employed by Zhang and coworkers could lead to a particularly efficient detection of the fast channel in spite of the slow contribution. Since our own detection technique, velocity map imaging (VMI), is similar to that used by Fischer and co-workers – differing only in the resonance enhanced multiphoton ionization (REMPI) scheme employed for the detection of the hydrogen atoms – and the photolysis wavelength that we used is closer to that of Zhang and co-workers, a good chance to clarify those differences and set the balance towards one or the other was ahead of us.

With such motivation in mind, we carried out experiments at the excitation wavelengths of 243 nm and 201 nm for photoexcitation into the 3s and 3p Rydberg states, respectively.[5] Ethyl radicals were produced either by flash pyrolysis from *n*-propyl nitrite, as in Fischer *et al.*'s work,[15] or by *in situ* photolysis of a precursor, ethyl iodide. While pyrolysis is known to produce radicals with some rotational excitation, the photodissociation of ethyl iodide[21] produces an ethyl radical with considerably larger ro-vibrational energies of around $\sim$0.6 eV and $\sim$1.3 eV at 243 and 201 nm, respectively. Similar results for photodissociation at 243 nm (the photodissociation of ethyl from the 3s Rydberg state) were obtained for the two sources of ethyl radicals. The comparison of our results with those previously reported by Zhang's group and Fischer's group at similar excitation wavelengths showed some discrepancies in both the branching ratio between the fast and slow channels as well as in the average energy position of the fast contribution. We therefore concluded that the initial internal energy content of the radical does not play any role in the photodissociation and more precisely in the dynamics at the conical intersection. In contrast, a slightly different excitation energy could be the source of a different dynamics, although a more detailed investigation will be necessary. Even more remarkable were our results on the photodissociation from the 3p Rydberg state at 201 nm.[4] An expected Boltzmann profile claimed the low energy part of the H-atom translational energy distribution, but what was more significant is the unique contribution observed when the CD_3CH_2 species was studied in the H-atom elimination channel. A site-specific C–H fast dissociation associated with the CH_2 moiety (the α carbon, C_α) dominated the distribution. The site-specific mechanism was rationalized in terms of two curve crossings, namely, a non-adiabatic crossing between the 3p Rydberg state, initially populated, and a valence state and a subsequent conical intersection with a second valence state.

The results would not be so impressive if it were not for the fact that they depend strongly on the way the ethyl radicals are generated. In addition to the *in situ* photolysis experiments (using the same laser pulse for the excitation of the ethyl radical and the detection of the H-atoms), we carried out a set of pyrolysis experiments and the results were, once again, unanticipated. The measured H-atom translational distributions in the photodissociation experiments at 201 nm[5] evidenced the key role of the internal energy of the parent radical in the process. Radicals with a smaller ro-vibrational energy, as those generated by pyrolysis right at the supersonic expansion of the molecular beam, do not have access to the rich curve-crossing region of the potential energy landscape. The radicals, excited only with the energy provided by the excitation photon and with the low internal energy, internally convert towards lower energy states, where statistical dissociation occurs, building up the Boltzmann contribution in the H-atom translational energy distribution. On the other side, the internal energy inherited by the radicals in the *in situ* 201 nm photogeneration process from the ethyl iodide precursor suffices to reach the curve-crossing region where they might undergo fast dissociation according to the mentioned site-specific mechanism.[4] At 243 nm excitation, the results – with no essential difference between the pyrolysis and photolysis experiments – provide a lower threshold for the first non-adiabatic crossing.

With all these results in our hands, one thing became clear: we needed a theoretical base to rationalize the experimental results. The theoretical description of the site-specific mechanism was, however, not trouble-free either. We knew that both the C_α-H and C_β-H dissociation channels should be simultaneously investigated. The *ab initio* electronic structure calculations for the C_α-H cleavage would provide a dissociation pathway through a repulsive surface which might just not exist in the picture associated with the C_β-H coordinate. The calculations must, in addition, include those Rydberg states expected to take part in the dynamics. The main difficulty was, in fact, the choice of the appropriate orbital set for the active space to produce smooth continuous potential energy curves (PECs) – and consequent homogeneous calculations – to reproduce both

dissociation channels. The problem resided in the Rydberg orbitals. If the calculations were to include the corresponding symmetry (plane or twist), the Rydberg orbitals considered ought to be different for both channels. Since the comparison between both systems was the priority, the decision of keeping the same set of orbitals for both coordinates and perform the calculations without symmetry was taken.[4,5,7]

The theoretical results were highly satisfactory. The *ab initio* calculations reported, for instance, in ref. 4 consider a dissociation pathway along the C_α-H coordinate through a repulsive surface, in which a conical intersection and a non-adiabatic crossing play a relevant role. Furthermore, the calculated *ab initio* PECs exclude any dissociation channel for the C_β-H coordinate, but suggest a slow decomposition on the ground state following non-radiative decay.

Once the site-specific dissociation channel was well established and understood for the ethyl radical, questions regarding the possible extrapolation to other similar radicals arose. Therefore, the next step was to investigate the site-specific H-atom elimination mechanism in the photodissociation of larger alkyl radicals, such as the propyl and butyl radicals. In a recent publication, we proved that the site-specific H-atom elimination mechanism is sufficiently robust to survive, and even to prevail, when the carbonated structure backbone is extended.[7] The experiments on alkyl radicals were the workbench to test another of the main ideas behind the site-specific H-atom elimination mechanism, namely, the role of the promoting mode channeling prompt H-atom dissociation. Taking into account the requirement of substantial initial internal excitation in the radical, an important redistribution of the available energy into different degrees of freedom had been expected, which should result in broad translational profiles where the statistical and fast contributions would merge. In contrast, the fast distributions obtained in all cases present a sharp Gaussian-type structure, typical of a prompt dissociation. The energy randomization failure brings to light the major role of the so-called vibrational promoting modes, which channel the dissociation through specific pathways and prevent the internal redistribution of the rovibrational energy (IVR). Such modes are usually characterized by larger Franck–Condon factors during absorption and possess the appropriate geometrical configuration to overcome the tight geometry restrictions imposed by the conical intersection.[7]

As a natural continuation of our previous works[4,5,7] where we have investigated the H-atom elimination from the ethyl isotopologues, in this work we extend the study to the detection of deuterium (D) atoms in the photodissociation of totally and partially deuterated species, such as CD_3CD_2, CH_3CD_2 and CD_3CH_2. We have carried out the study at the previously used excitation wavelength, ~201 nm, and extended to 193 nm, to test the requirement of the radical internal energy to promote site-specific photodissociation channels. In Section 2, the theoretical and experimental methodologies are explained. In Section 3, the main experimental results are exposed which are discussed in the light of the theoretical results. The main conclusions are presented in Section 5.

2. Methods

2.1 Experimental

Two different laboratories were involved in the present work. The experiments at around 201 nm were carried out in Madrid and the experiments at 193 nm were carried out at FORTH-IESL in Crete.

2.1.1 Excitation at 201 nm. In Madrid,[2,4,22] the laser system consisted of two Nd:YAG (Quanta Ray Pro 190) pumped dye lasers (Sirah Cobra-Stretch). One laser system (pump) was tuned at ~201 nm produced by sum-frequency mixing in a nonlinear crystal to combine the fundamental and the second harmonic radiation and used for both *in situ* photolysis and photoexcitation to the 3p Rydberg state. The other laser (probe) was set up at around ~365 nm for the detection of the hydrogen $H(^2S)$ and deuterium $D(^2S)$ atoms using the $2p(^2P_{1/2}) \rightarrow 1s(^2S_{1/2})$ (3 + 1) REMPI scheme. The radiation produced around 201 nm (~0.15 mJ per pulse) was employed, as well, for the *in situ* generation of the ethyl radicals through photolysis of ethyl iodide. The pump wavelengths were tuned at 201.2, 200.8, 200.3 and 200.15 nm to excite the 0_0^0 origin of the B-band of the corresponding precursors, *i.e.* CH_3CH_2I, CH_3CD_2I, CD_3CH_2I and CD_3CD_2I, respectively, to ensure the maximal formation of CH_3CH_2, CH_3CD_2, CD_3CH_2 and CD_3CD_2 radicals. This *in situ* photolysis has shown to produce ethyl radicals with a substantial amount of internal rovibrational energy.[4,21] The probe pulse was set at 364.8 nm for $H(^2S)$ detection and at 364.5 nm for $D(^2S)$ detection. The laser pulses were delayed 10 ns to guarantee the efficient detection of the hydrogen/deuterium-atoms while avoiding any "fly out" process (see below).

The iodated precursors of ethyl radicals, purchased from Sigma-Aldrich, were seeded in helium (10%, 1 atm backing pressure) and expanded into vacuum using a pulsed nozzle (General Valve Series 9, 0.5 mm orifice). The collimated gas pulse (Beam Dynamics skimmer, Standard Model 2, 0.5 mm diameter orifice) was intersected in the ionization chamber by the focused (focal length f = 25 cm) laser pulses.

An homogeneous 6 kV electric field (VMI single-field) was used to accelerate the H^+/D^+ ions through a field-free time-of-flight (TOF) region (45 cm) before hitting the impedance matched microchannel plates (Chevron configuration, 40 mm diameter). The resulting electron avalanche strikes a phosphor screen (P47), thereby creating the ion image, which is recorded using a CCD camera (SONY 1024 × 768 pixel) controlled using National Instrument (NI) LabView 7.1 and IMAQ VISION software.

The velocity map H^+ images are quadrant symmetrised and Abel inverted using the Hankel transform, prior to extracting the translational energy and angular distributions. The independent velocity–radius calibration of the apparatus is done by measuring resonantly ionized CH_3 ($\nu = 0$) fragments produced after the photodissociation of CH_3I at 333.45 nm (one color pump–probe experiment) at different repeller potentials, taking advantage of the well known kinetic energy release of the $I(^2P_{3/2})$ yielding channel at this photolysis wavelength.

We note that in all the experiments shown here from both laboratories, images are recorded using a parallel polarization configuration with respect to the detector plane of both the pump and probe lasers. However, images have also been recorded using a perpendicular polarization setup of both lasers in order to check the detector response as well as the alignment.

2.1.2 Excitation at 193 nm. Since the pulsed gas generation and ion detection implementation are similar to the set-up in Madrid, only the main differences at FORTH-IESL lying in the laser system and, therefore, in the generation and excitation of the radicals studied will be described. Ethyl radical generation and subsequent excitation were carried out at 193 nm using an ArF Lambda Physik COMPEX excimer laser. The produced H(^{2}S) and D(^{2}S) atoms were ionized (using the same 2p($^2P_{1/2}$) $\leftarrow$ 1s($^2S_{1/2}$) (3 + 1) REMPI scheme at 364.8 nm and 364.5 nm, respectively) using a XeCl excimer pumped dye laser (Lambda Physik LPD3000). The time delay between the pump and probe pulses was carefully adjusted for each set of experiments between 5 and 10 ns to simultaneously avoid H/D-atom "fly out" from the interaction region of the VMI spectrometer and multiphoton ionization (MPI) processes.

The "fly out" process where the probed species leave the laser interaction region partially before the probe laser pulse arrives is a usual problem in the detection of light species, such as H- and D-atoms. To avoid such undesirable effects, the time delay between the pump and probe pulses must not exceed a few nanoseconds. The problem of working with a small time delay between nanosecond lasers is, however, the generation of multiphoton absorption processes, where the studied species can absorb photons simultaneously from both the pump and probe laser pulses. In both laboratories, a careful analysis of the image as a function of the time delay was performed to optimize the signal while avoiding both parasite effects.

2.2 Theoretical

The potential energy curves (PECs) of the different electronic states were obtained using state-averaged complete active space self-consistent field (SA-CASSCF) calculations followed by internally contracted multi-reference configuration interaction (MRCI) calculations available in the MOLPRO package.[23] For this system, it has been found that the Davidson correction becomes unstable for the excited states probably due to strong couplings between them. Therefore, no correction to the size inconsistency of MRCI has been included. The active space used for these calculations consists of 13 electrons in 10 orbitals, the two first orbitals being kept closed (those associated with the 1s orbitals of the two carbon atoms). Ideally, the ethyl radical can be described in the C_s symmetry group. However, in order to characterize the dissociation pathways to the different asymptotes corresponding to H-atom elimination, two possible symmetry planes may arise for torsion angles ϕ = 0° and 90°. Since the description of the electronic wave function calculated using multi-reference methods is very sensitive to the orbitals included in the active space, it is important to use the same active space for the different PECs leading to the different fragments in both the Franck–Condon and the asymptotic regions. To avoid mismatches between the symmetries of the different electronic states (the ground state switches from A' to A'' under a torsion of 90°) and to ensure that the active space always includes the same orbitals, the calculations were performed without symmetry.

The ethyl radical is composed of seven atoms and thus possesses fifteen degrees of freedom. The purpose of the calculations is to obtain a simple (one dimensional) representation of the energetics of the involved electronic states as a function of R_{CH} and the distance between the dissociating hydrogen atom and its corresponding carbon atom. A partial relaxation of the ground state of the radical has been performed at the CASPT2 level at each R_{CH} distance between 0.6 and 5 Å for all the dissociation channels considered. This presents the advantage to match the dissociation energy of the ground state, always keeping in mind that the calculated path is not necessarily the most favorable for the excited states. The MRCI calculations of the excited states were then performed over the obtained ground state geometries.

Diabatization was later carried out using the model presented in ref. 2 and 3. This method consists of estimating geometrically the mixing angles between the different states along the reaction coordinate that allows to pass from the adiabatic to the diabatic representation. The non-adiabatic coupling matrix elements (NACMEs) between the different states (not shown here) were obtained as the derivative of the corresponding mixing angle as a function of the chosen coordinate, in this case, the C–H bond. They were published in previous works[4,8] allowing us to identify conical intersections and avoid crossings characterizing the reaction pathways.

In order to obtain an estimate of the internal energy of the radical and products, anharmonic zero-point energies were calculated for the ethyl (CH_3CH_2) radical, carbene (CH_3CH) and ethylene (CH_2CH_2). Vibrational anharmonic fundamentals were computed using vibrational second order perturbation theory (VPT2)[24] as implemented in Gaussian,[25] to estimate the zero-point vibrational energies. The corresponding full-dimensional anharmonic force field was computed using second order Möller–Plesset theory (MP2).[26] For all calculations, the aug-cc-pVTC basis set of Dunning was used for the C and H atoms.

Finally, the most relevant conical intersections were also optimized at an *ab initio* level. In our approach, all the geometry optimizations are performed in the ground state. A specific optimization is therefore necessary in order to estimate more accurately the minimum energy for the conical intersection seam, and therefore the most favorable geometry to access it. Besides the intrinsic cost of the complex algorithms employed to locate a seam, it involves a large number of degrees of freedom, since the seam has 3*N*-6-1 dimensions (where *N* is the number of atoms). The optimization was thus performed in two steps. First, the conical intersection is optimized at the CASSCF level, where analytical gradients are available. Then, only the coordinate of interest (C–H distances in our case) is sampled with a very large density of MRCI points around the

optimized value. The geometries optimized using this procedure allow us to confirm the conical intersections extracted by our diabatization algorithm. In addition, the comparison between these geometries and the ones used in our potential energy curves gives information on the energy position of the seam. If the change in geometry is significant for a given conical intersection, it will imply that it lies at a lower energy than depicted. Therefore, a certain vibrational mode can help to drive the molecule toward the minimum of the seam and promote its access.

3. Results

Relevant reaction pathways along the C_α-H and C_β-H reaction coordinates following the photoexcitation of ethyl radicals are summarized in the energy level diagram depicted in Fig. 1. Based on the *ab initio* calculations reported in ref. 4, 5, 7 and in this work, the first excited electronic states of the ethyl radical along with the open dissociation channels are shown. While one-photon absorption in the 201–193 nm range drives the radical into the $\tilde{B}\ ^2A'(3p)$ Rydberg state, five dissociation channels have been identified:

- C_α-H dissociation into $CH_3CH(1\ ^1A')$, labeled as **1a**
- C_α-H dissociation into $CH_3CH(1\ ^1A'')$, labeled as **1b**
- C_α-H dissociation into $CH_3CH(2\ ^1A')$, labeled as **2a**
- C_β-H dissociation into CH_2CH_2 $(2\ ^1B_2)$, labeled as **2b**
- C_β-H dissociation into CH_2CH_2 $(1\ ^3B_1)$, labeled as **2c**

Mechanism **1b** corresponds to the C_α site-specific dissociation reported in our previous work[4,7] following photoabsorption at 201 nm while **1a** represents the already reported C_α radiationless decay followed by statistical dissociation. We note that channel **1a** is characterized by an efficient randomization of the energy through several avoided crossings, and further dissociation after internal conversion into the 3s Rydberg state or to produce $CH_3CH(1\ ^1A')$. Reaction pathways labeled as **2a**, **2b** and **2c** can be accessed at 193 nm and are discussed here for the first time.

Fig. 2 shows a series of Abel-inverted images corresponding to $H(^2S)$ (top row) and $D(^2S)$ (bottom row) atoms produced in the photodissociation of CH_3CH_2 radicals and in the partially or totally deuterated isotopologues, CD_3CH_2, CH_3CD_2, and

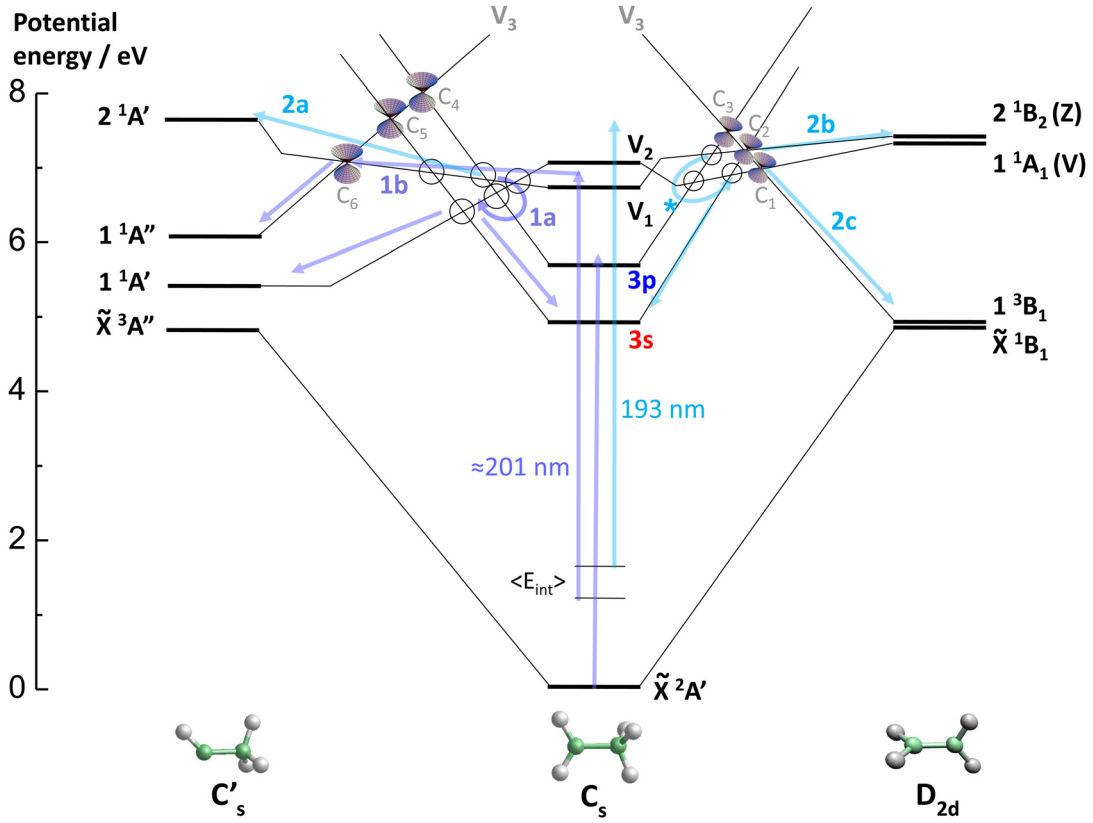

Fig. 1 Energy level diagram based on the *ab initio* calculations presented in this work and those of ref. 4. The C_s electronic states of the ethyl radical are shown in the central part of the figure. These include the $1\ ^2A'(3s)$ and $2\ ^2A'(3p)$ Rydberg states and two valence states, labeled as V_1 and V_2. Excitation energies corresponding to ≈201 nm and 193 nm are represented by vertical arrows departing from the internal energy level of the radicals. The different dissociation pathways along the C_α-H (left) and C_β-H (right) reaction coordinates are labeled as 1a (C_α radiationless decay at 201 nm), **1b** (C_α site-specific H-atom elimination at 201 nm), **2a** (C_α site-specific H-atom elimination at 193 nm), 2b (C_β site-specific H-atom elimination at 193 nm), and 2c (C_β site-specific C–H dissociation at 193 nm). Double cones represent conical intersections and circles represent avoided crossings. The initial internal energies, $\langle E_{int}\rangle$, of the ethyl radical arising from the *in situ* photolysis of the precursor used at the two excitation wavelengths, ≈201 nm and 193 nm, are also indicated. See the text for details.

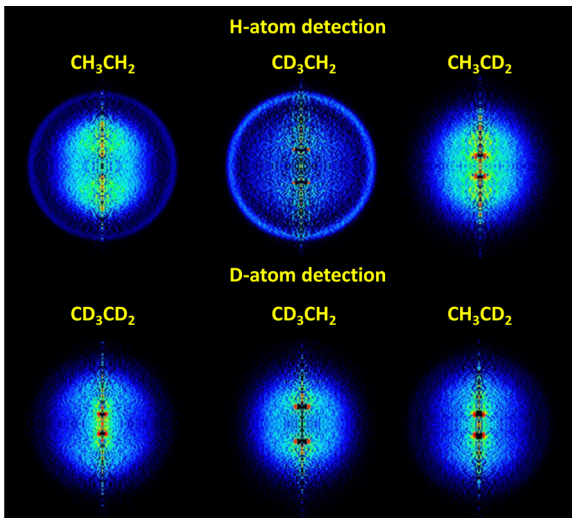

Fig. 2 H-atom (top) and D-atom (bottom) Abel-inverted velocity map images for the four isotopologues CH_3CH_2, CD_3CH_2, CH_3CD_2 and CD_3CD_2 excited at 201.2 nm, 200.8 nm, 200.3 nm and 200.15 nm, respectively.[4]

CD_3CD_2. The H-atom images and the corresponding total translational energy distributions (TEDs) shown in Fig. 3 constitute the cornerstone of the site-specific mechanism as they were first published in our original work on the matter in ref. 4. While the sharp peak observed at higher energies was assigned to the site-specific C_α-H dissociation, *i.e.* channel **1b**, the Boltzmann contribution is attributed to statistical dissociation following internal conversion into low-lying electronic states,

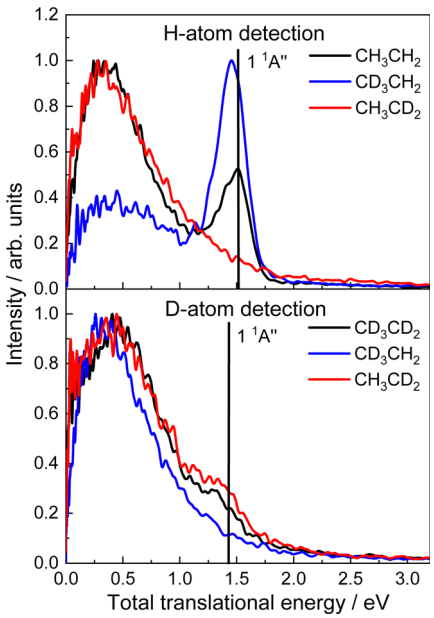

Fig. 3 Top: total translational energy distributions (TEDs) extracted from the H-atom Abel-inverted images in Fig. 2 (top). Bottom: TEDs extracted from the D-atom Abel-inverted images in Fig. 2 (bottom). Vertical bars indicate the available energy for the C_α dissociation limit, *i. e.* $H(^2S)$ + $CH_3CH(1\ ^1A'')$.

occurring either through the 3s Rydberg state or through the formation of $CH_3CH(1\ ^1A')$, labeled as channel **1a**.

The D-atom images and TEDs (shown as well in Fig. 3) were taken at that time for a further confirmation of the proposed mechanism. If we were expecting an unquestionable confirmation of the site-specific dissociation mechanism, the $D(^2S)$ results were highly discouraging. While in the $H(^2S)$ images, the site-specific feature, namely a sharp highly-recoiled ring, was clearly visible for the CH_3CH_2 and CD_3CH_2 species, and non-existing for the CH_3CD_2 radical – confirming the cleavage of the C_α-H bond – the $D(^2S)$ images obtained from the CH_3CD_2 and CD_3CD_2 species showed no clear sign of a possible fast dissociation channel. The corresponding TEDs shown in Fig. 3, however, gave us hope back since the Boltzmann component of the TEDs showed a clear "bump" in the energy region where the fast contribution was expected. These observations seem to point towards the decrease of the zero-point energy (ZPE) as a result of the substitution of H-atoms by D-atoms. The location in the geometry and energy of the conical intersection does not change with the isotopic substitution. In contrast, the smaller ZPE implies that, in comparison with the non-deuterated species, a higher excitation in the C–D mode would be required to access the non-adiabatic crossing and the conical intersection. At the same excitation energy, the D-atoms would therefore have a smaller probability to access the conical intersection and thus to be produced through the site-specific dissociation pathway **1b**. In addition, the higher mass of the D-atom leads to a higher density of states, thus fostering the internal conversion, contributing to channel **1a**, as always present the competing mechanism. The fact that mechanism **1b** is solid enough to persist when the alkyl chain is modified further supports these arguments to explain the results in Fig. 3.

The pyrolysis *vs.* photolysis experiments published in our previous paper on the 3s *vs.* 3p photodissociation dynamics of the ethyl radical,[5] which demonstrated the capital role of the radical internal reservoir, suggested just an internal energy-based issue as the reason behind the lack of a clear fast dissociation feature. For the deuterated species, the energy provided by the 201 nm photon plus the internal energy inherited in the dissociation of the precursor might not be sufficient to reach the curve-crossing region.

If we need wavelengths shorter than 200 nm, the answer was at FORTH-IESL in Crete, where we have already harvested relevant results.[27] This laboratory is provided with excimer lasers able to generate radiation at 193 nm, which should be more than enough to test our hypothesis, as suggested by the early experiments of Zhang and coworkes.[14]

Once in Crete, a new set of experiments were carried out for all isotopomers at 193 nm and $H(^2S)/D(^2S)$ (3 + 1) REMPI detection at ~364 nm. The results are shown in Fig. 4 and 5. The $H(^2S)$ (top) and $D(^2S)$ (bottom) Abel-inverted images obtained from CH_3CH_2 and CD_3CD_2, respectively, depicted in Fig. 4, are almost indistinguishable, both similarly showing the sharp highly recoiled ring and a central diffuse disk, mirrored in the corresponding TEDs as the sharp peak at high translational energies and the Boltzmann-type contribution. The extra

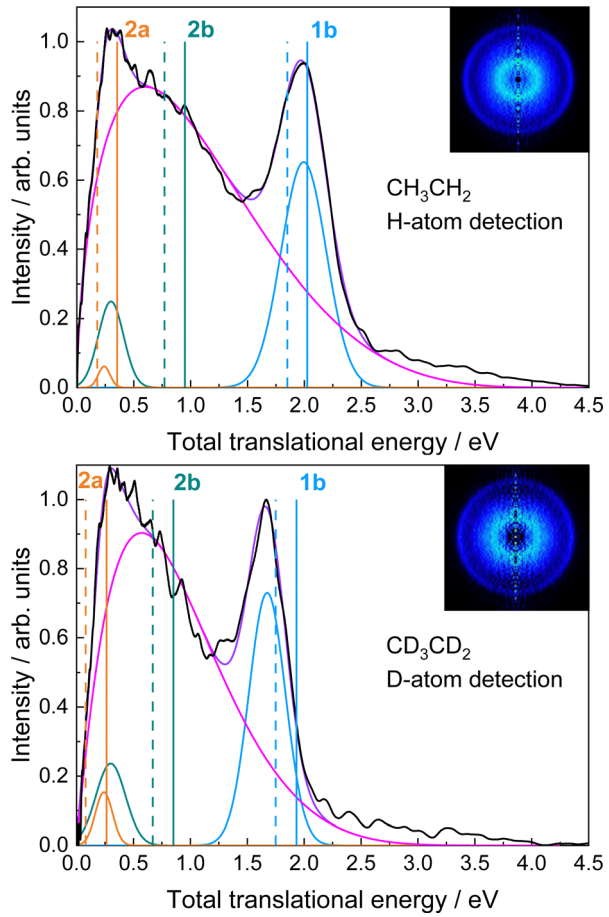

Fig. 4 H-atom (top) and D-atom (bottom) Abel-inverted velocity map images for the CH_3CH_2 and CD_3CD_2 radicals, respectively, photoexcited at 193 nm above the 3p Rydberg state and the corresponding total translational energy distributions (TEDs). Vertical bars indicate the available energy for the $H(^2S)$ + $CH_3CH(1\ ^1A'')$ (channel **1b**, blue) and $H(^2S)$ + $CH_3CH(2\ ^1A')$ (channel **2a**, orange) for the H-atom elimination (or D-atom elimination) from C_α and for the $H(^2S)$ + CH_2CH_2 ($2\ ^1B_2$ (Z)) (channel **2b**, dark cyan) photodissociation channels. The two different cases considered for the initial internal energy of the ethyl radical are represented by dashed and full lines (see the text). The TEDs were fitted to three Gaussian-type distributions, one for each channel energetically open, and to a Boltzmann-type distribution (pink curve).

energy provided by the 193 nm photon (with respect to the 201 nm photon) clearly enables the site-specific mechanism for the deuterated species. In addition, the high energies employed in the experiment have brought new interesting dynamics as reflected in the images by an inner sharp ring. The low-energy region of the TED shows indeed a richer structure in comparison with the 201 nm experiment (Fig. 3). Since the Boltzmann contribution obscures this area, a deconvolution analysis of the distribution profiles shown in Fig. 4 to extract information about the possible new dissociation pathways involved is required.

The first step for the deconvolution analysis was to set energy references for the asymptotic dissociation limits established by the theoretical calculations. Besides the sharp peaks located at ~2.0 and ~1.7 eV for the CH_3CH_2 and CD_3CD_2 radicals, respectively, assigned to the H + $CH_3CH(1\ ^1A'')$ and D + CD_3 $CD(1\ ^1A'')$ dissociation channels (channel **1b**), landmarks are tentatively set for two additional channels corresponding to H/D cleavage from C_α yielding H + $CH_3CH(2\ ^1A')$/D + CD_3 $CD(2\ ^1A')$ (channel **2a**) and from C_β yielding H + CH_2CH_2 ($2\ ^1B_2$(Z))/D + CD_2CD_2 ($2\ ^1B_2$(Z)) (channel **2b**). The references, represented in Fig. 4 by vertical bars, denote the available energy, E_{av}, for each photodissociation channel and can be derived according to

$$E_{av} = h\nu + E_{int}(C_2H_5) - D_0 \quad (1)$$

where $h\nu$ is the photon energy, $E_{int}(C_2H_5)$ is the internal energy of the ethyl radical (or the corresponding isotopologue) produced by the *in situ* photolysis of the precursor, ethyl iodide, and D_0 is the C–H bond dissociation energy. To the best of our knowledge, there are no data regarding the energetics of the 193 nm dissociation of ethyl iodide and, therefore, no information relative to the term E_{int} (C_2H_5) is available. Two references corresponding to two limiting cases have therefore been introduced for each channel. In the first case, it is assumed that the fraction of the total energy going into internal energy of the ethyl radical, f_{int}, does not depend on the excitation energy. Considering such assumption, the dashed vertical bars showed in Fig. 4 are calculated from eqn (1), assuming a f_{int} value of 0.44, as obtained in the photodissociation of ethyl iodide in the origin of the B-band[21] at 201.2 nm. In the second case, the extra amount of energy provided by the 193 nm photon with respect to the 201.2 nm excitation is assumed to be channeled into the internal energy of the ethyl radical. The resulting E_{av} obtained from eqn (1) is represented in Fig. 4 and 5 by solid bars.

The second step of the analysis was to fit the experimental translational energy distributions. Since the images show two sharp peaks and one large diffuse central disk, two Gaussian functions and one Boltzmann-type function would seem appropriate to fit the corresponding TEDs. However, based on the available energies, the inner sharp ring cannot be unequivocally assigned to either channel **2a** or channel **2b**. We therefore use three Gaussian functions to consider the three open fast dissociation channels, **1b,** at higher translational energies and **2a** and **2b** at low energies. In addition, the following function is used to fit the Boltzmann-type broad contribution assigned to channel **1a:**

$$I(E_T) = AE_T^i(1 - E_T)^j \quad (2)$$

where E_T is the translational energy and A, i and j are fitting parameters which do not contain physical meaning. This function was described first by Muckermann[28] and lately used in different photodissociation investigations taking advantage of its simplicity.[29,30] We note that employing a Boltzmann function could give rise to some physically interesting information, but it requires prior knowledge of physical parameters, such as the rotational temperature, and it is beyond the scope of the present work. Although not conclusive, the results of the fit shed some light on the dynamics involved. As shown in Fig. 4, the fit for the CH_3CH_2 and CD_3CD_2 species reproduces satisfactorily the measured translational energy distributions.

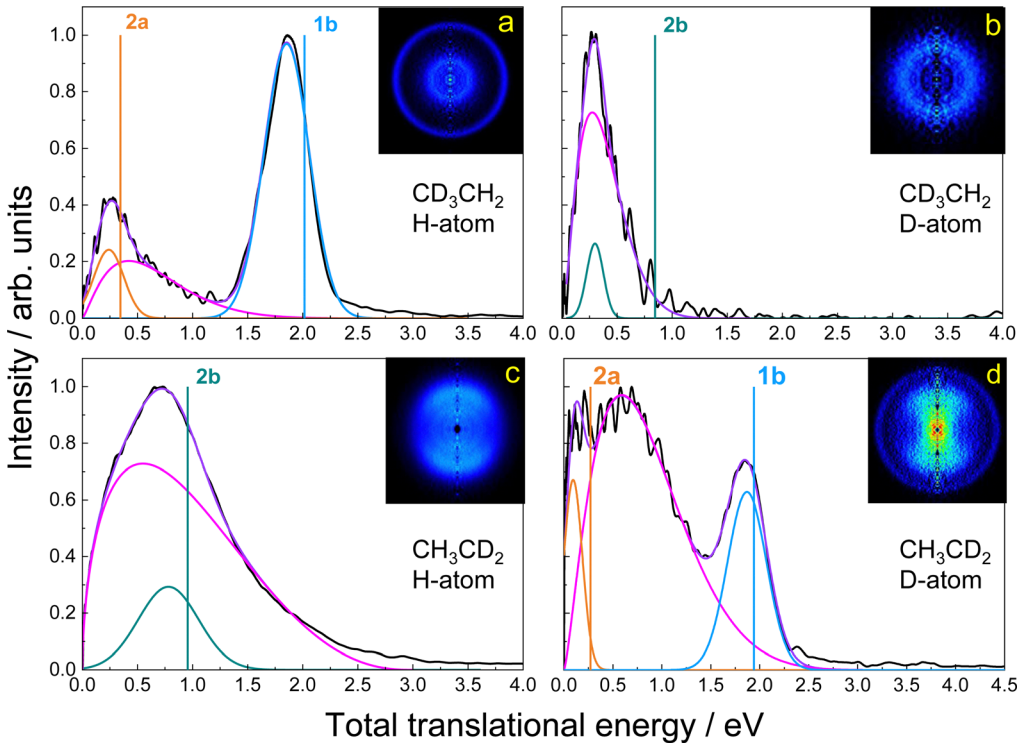

Fig. 5 H-atom Abel-inverted velocity map images for the CD_3CH_2 (a) and CH_3CD_2 radicals (c). D-atom Abel-inverted images for the CD_3CH_2 (b) and CH_3CD_2 radicals (d), photoexcited at 193 nm above the 3p Rydberg state and the corresponding total translational energy distributions (TEDs). The available energy is represented as vertical bars for $H(^2S)$ + $CH_3CH(^1\,^1A'')$ (channel **1b**, blue) and $H(^2S)$ + $CH_3CH(2\,^1A')$ (channel **2a**, orange) for the H-atom elimination (or D-atom elimination) from C_α and for the $H(^2S)$ + CH_2CH_2 ($2\,^1B_2(Z)$) (channel **2b**, dark cyan) photodissociation channels. These bars consider the initial internal energy of the ethyl radical obtained from the second case only (see text). The TEDs were fitted to different Gaussian distributions, one for each channel energetically open, and to the Boltzmann-type distribution (pink curve).

At high translational energies, a sort of tail is observed on the experimental data and not reproduced by the fit. This structure might reflect some minor contributions of the dissociation channel **2c**, leading to the formation of CH_2CH_2 or CD_2CD_2 ($1\,^3B_1$) following C_β-H cleavage. Available energies of 3.53 and 3.36 eV (3.43 and 3.26 eV for the deuterated species) are however expected for this channel depending on the case considered for the initial E_{int} of the radical while the tail is observed for energies even above 4 eV. Taking into account that eqn (2) can be used only to qualitatively reproduce the Boltzmann-type contribution, this tail must mostly reflect part of channel **1a**, not properly fitted.

The results of the deconvolution analysis for the partially deuterated isotopomers, CD_3CH_2 and CH_3CD_2, for both H-atom and D-atom detection, confirmed the former assignments and discussions and provided additional information. Evidence of the C_α H/D-atom site-specific dissociation mechanism is dramatically visualized for the CD_3CH_2 radical, as shown particularly in Fig. 5(a) and (b), due to the fact that the Boltzmann contribution in both cases is largely reduced in comparison to the other three isotopomers. We notice that, at 193 nm excitation, two sources can contribute to the Boltzmann-type component of the TEDs: slow statistical dissociation first from the $C_\beta H_3/C_\beta D_3$ moiety (indicated as * in Fig. 1), and second from the C_α-H/C_α-D dissociation marked as **1a** in Fig. 1. Oddly enough, while by comparing Fig. 5(a) and (c), the dissociation on the $C_\beta H_3/C_\beta D_3$ moiety seems to constitute the major source of slow H/D-atoms, and the comparison of Fig. 5(b) and (d) would seem to indicate that the frustrated C_α-D/H dissociation represents the main contribution to the Boltzmann component.

A noteworthy aspect of the TEDs shown in Fig. 5 is the non-Boltzmann shape of the slow contribution. Boltzmann-like profiles denote diabatic decomposition processes in which the energy acquired by the parent species in the excitation step is randomly distributed among the internal degrees of freedom, resulting in slow – low translational energy – products with a rovibrational statistical distribution. The deconvolution analysis reveals, therefore, new dissociation pathways open at 193 nm which overlap with the slow component of the distributions but possess a non-statistical nature. In Fig. 5a, and d, the new contribution must be necessarily associated with channel **2a**: a site-specific dissociation channel in the C_α moiety, yielding $H(^2S)$ + CD_3 $CH(2\,^1A')$ and $D(^2S)$ + CH_3 $CD(2\,^1A')$ products, respectively. In Fig. 5d, the new contribution is observed at very low recoils, despite the large Boltzmann contribution observed in this case. More obscure but more striking as well is the site-specific dissociation in the C_β moiety, channel **2b**, observed in Fig. 5b and c representing D/H-atom detection from the CD_3CH_2/CH_3CD_2 radicals.

4. Discussion

The energy diagram represented in Fig. 1 summarizes the different dissociation pathways for the photoexcited ethyl radical. The electronic states of the ethyl radical are located in the central part of the diagram. Five doublet A′ or A″ (C_s symmetry) electronic states are considered in this work: the 3s ($\tilde{A}\ ^2A'$) and 3p ($\tilde{B}\ ^2A'$) Rydberg states and three valence states, labeled here as V_1, V_2 and V_3. While V_2 and V_3 are characterized by A′ and A″ symmetries, respectively, both the ground state and V_1 change its symmetry from A′ to A″ depending on the torsion angle between the CH_2 and the CH_3 moieties. Computed transition dipole moments (see ref. 4) show that the absorption into the 3s and 3p states is considerably larger than those of the valence states.

Dissociation limits in terms of the different electronic states of the CH_3CH and CH_2CH_2 co-fragments are depicted in the left and right sides of Fig. 1, respectively. Conical intersections and avoided crossings identified in the computed potential energy curves and NACMEs reported previously[4,5,7] are also indicated. An $\langle E_{int}\rangle$ of 1.27 eV corresponding to f_{int} = 0.44[21] at 201 nm photon energy is shown. A value of 1.53 eV is used for the excitation at 193 nm, reflecting that all the extra energy provided by this photon with respect to the 201 nm photon is considered to be channeled into internal energy. We note that all the mechanisms discussed for the 193 nm excitation are also opened if an internal energy corresponding to f_{int} = 0.44 is considered.

Dissociation upon absorption at 201 nm of the pyrolysis-generated ground state ($\tilde{X}\ ^2A'$) ethyl radicals is explained through internal conversion from the pumped Rydberg 3p state to lower energy levels where the statistical dissociation may occur. While radicals generated by pyrolysis often have some rotational excitations, the ro-vibrational energy amount of photolysis-generated radicals depends on the reaction used. The ethyl radicals produced here by the *in situ* photolysis of ethyl iodide are characterized by a considerably larger $\langle E_{int}\rangle$ and thus possess enough energy -- the total of the photolysis energy and $\langle E_{int}\rangle$ – to reach the energy region located between 6 and 7 eV, characterized by a large amount of curve crossings between the 3p and several valence states. The strong couplings associated with the non-adiabatic crossings and conical intersections facilitate the transfer of population between the corresponding states, leading to two possible dissociation pathways. A fast non-adiabatic crossing between the Rydberg 3p and the V_1 valence states and a subsequent conical intersection, labeled as C_6 (Fig. 1), would steer the excited ethyl radicals to dissociate into electronically-excited $CH_3CH(1\ ^1A'')$ products. Such a path is labeled as mechanism **1b** in Fig. 1. The repulsive dissociation mechanism described – namely, the site-specific H-atom dissociation mechanism – competes with internal conversion to lower lying electronic states in which the statistical dissociation would occur either through the 3s Rydberg state or through the formation of $CH_3CH(1\ ^1A')$ (mechanism **1a** in Fig. 1). Mechanism **1a** explains the Boltzmann-type distribution observed in the TEDs while the high-recoiled sharp peak is attributed to the site-specific pathway **1b**. Both **1a** and **1b** mechanisms have been the focus of our previous publications on the subject.[4,5]

The extra amount of energy provided by the 193 nm photon in comparison with that by the ≈201 nm photon opens up the possibility of new dissociation channels, labeled as **2a** and **2b** in Fig. 1. In addition to the **1a** and **1b** mechanisms which remain active at this higher excitation energy (and constitute, actually, the major dissociation channels even at 193 nm), the direct dissociation through the V_1 valence state along the C_α-H coordinate would produce electronically-excited $CH_3CH(2\ ^1A')$ radicals (mechanism **2a**). Such a fast dissociation mechanism should compete with the similar fast **1b** dissociation path. Noteworthily, the available energy for the $CH_3CH(1\ ^1A'')$ (**1b**) and $CH_3CH(2\ ^1A')$ (**2a**) products is drastically different. The energy gap between the $1\ ^1A''$ and $2\ ^1A'$ states of CH_3CH greatly exceeds the extra amount of energy provided by the 193 nm photon (taking into consideration as well the differences between the $\langle E_{int}\rangle$ of the ethyl radicals produced at ≈201 and 193 nm). As a result, the $H + CH_3CH(2\ ^1A')$ feature (mechanism **2a**) appears at around 0.25 eV in the translational energy distribution (Fig. 5a).

At 193 nm, the ethyl radical possesses, on the other hand, enough energy to reach the non-adiabatic crossing between the Rydberg 3p state and V_1 valence state. A similar fast dissociation process along the C_β-H reaction coordinate would then lead to $H + CH_2CH_2/CH_2CD_2$ or $D + CD_2CD_2/CD_2CH_2$ (D_{2d} symmetry) in the $2\ ^1B_2(Z)$ excited state (mechanism **2b**), through the C_2 conical intersection. As in the case of the mechanism **2a**, the available energy for the $H + CH_2CH_2$ ($2\ ^1B_2(Z)$) channel (∼0.3–0.9 eV) results in an experimental feature that overlaps with the Boltzmann component of the translational energy distributions shown in Fig. 5. We note that once at C_2, the dissociation into ethylene in its triplet state (mechanism **2c**) is energetically open, but seems unfavorable based on our experimental results.

The relative intensity between the different contributions appearing in the TEDs in Fig. 4 allows us to conclude that at 193 nm the ethyl radicals are excited directly into high rovibrational levels of the 3p Rydberg state, in agreement with computed transition dipole moments.[4] As shown in Fig. 1, several electronic states are accessible at 193 nm. If excitation would take place in any of the available valence states, the non-adiabatic crossing between the 3p and the V_1 valence states, prior to the C_6 conical intersection, which eventually lead to the reported C_α site-specific mechanism[4] (labeled as **1b** in Fig. 1), would not occur. Such a situation should reduce dramatically the contribution of the C_α carbon to the statistical contribution of the corresponding TEDs. In other words, the radicals would be taken almost straightforwardly to the dissociative state. As clearly seen in Fig. 4, the situation is far from that case. Furthermore, direct excitation to high ro-vibrational levels of the 3p Rydberg state would necessarily favour the coupling with the valence states, justifying the fact that, at 193 nm, the reported site-specific mechanism **1b** remains the dominant contribution.

The similarities and differences between the four plots of Fig. 5 provide relevant information regarding the role of the curve crossings involved in the dynamics. In Fig. 5a, the onset of the **2a** component (low-recoiled H-atoms produced in correlation to $CD_3CH(2\ ^1A')$ products) coincides with the energy of the $2\ ^1A'$ state. In terms of the partition of available energy, such coincidence implies that the majority of the energy in excess of the excited ethyl radical is funneled into translational degrees of freedom of the products. In Fig. 5c and d, we observe that the same behavior is observed for the **2a** mechanism in CH_3CD_2 and for the **2b** mechanism in CH_3CD_2. The situation is largely different, however, for the CD_3CH_2 radical dissociation according to the **2b** mechanism.

The width of the distributions associated with the **2a** and **2b** mechanisms (in terms of full width at half maximum FWHM), which reflects the rotational energy distribution in the radical products, varies from $\sim$0.7 eV for CH_3CD_2 (H-atom detection, **2b** path) to $\sim$0.3 eV for CD_3CH_2 (H-atom detection, **2a** path) and CD_3CH_2 (D-atom detection, **2b** path) and to $\sim$0.2 eV for D-atom detection (**2a** path) in CH_3CD_2.

4.1 The role of the conical intersections

Rationalization of the observed experimental features into the corresponding proposed mechanisms must be carried out on the basis of solid theoretical calculations. The diabatic potential energy curves (PECs) computed as a function of the C–H bond distance leading to CH_2CH_2 (D_{2h}), CH_2CH_2 (D_{2d}) and CH_3CH (C_s) products are presented in Fig. 6. As mentioned before, symmetry was not taken into consideration in the calculations of the ethyl states. Thus, the comparison between the three dissociation channels is straightforward. In C_s symmetry, the ethyl 3s and 3p Rydberg states and the V_1, V_2 and V_3 valence states interact through the non-adiabatic couplings and conical intersections (tagged with light blue circles), which depend on the reaction coordinate. As discussed in our previous work[4] and as observed in Fig. 6 (upper panel), any prompt dissociation producing ethylene CH_2CH_2 (D_{2h}) is highly unlikely. This channel would only contribute to the statistical dissociation through internal conversion into low-lying electronic states. The picture provided by the potential energy curves along the different pathways, combined with the experimental results, allows us to confidently propose probable mechanisms and to provide a qualitative description of the competing processes.

In most of cases, conical intersections can be related to the symmetry breaking of the system, and the vibrational modes able to break the symmetry and facilitate couplings through the conical intersections are named "activation modes". In the case of ethyl, which the genuine symmetry group is C_s, the free torsional movement can be considered as an activation mode as it will permanently break the C_s symmetry and consequently will facilitate couplings at the conical intersections. In addition to these activation modes, some vibrational motions can sometimes favor one specific pathway against others. In such cases, we use the term "promoting modes".

The geometries extracted from the curves (Fig. 6) of the ethyl radical at the conical intersections relevant to this work are

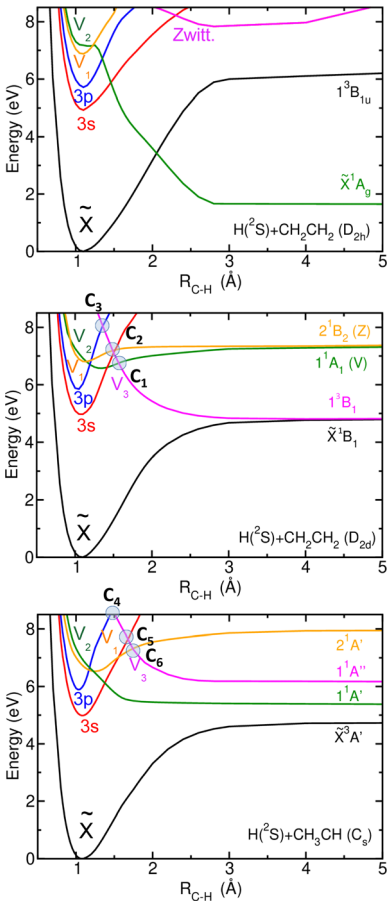

Fig. 6 Diabatic potential energy curves as a function of the C–H distance leading to H + CH_2CH_2 (D_{2h}) (upper panel), H + CH_2CH_2 (D_{2d}) (middle panel), and H + CH_3CH (C_s) (lower panel) which include the three fast dissociation channels discussed in Fig. 1. The color key for the three panels is as follows: black lines represent the ground state; red and blue lines represent the 3s and 3p Rydberg states, respectively; orange, green and magenta lines represent the valence states in the increasing order of the Franck–Condon vertical excitation energy; light blue circles represent the conical intersections found between the indicated excited states, labelled as C_1 to C_6.

represented in Fig. 7 in comparison with the optimized *ab initio* structures. The change of the geometry parameters – angles and distances – from the *ab initio* structure to the conical intersection geometry provides information on the role played by the vibrational modes in the dissociation dynamics. The potential energy curves computed here and plotted in Fig. 6 follow the minimum energy path of the ground state. If the minimum energy path for a given excited state is similar to the one for the ground state, the optimized *ab initio* geometry of the conical intersection will be similar to the geometry extracted from the curves. In contrast, if the minimum energy path for a given excited state is significantly different from the ground state, the optimized *ab initio* geometry of the conical intersection will be completely different from the one considered in the curve. This implies that the real energy position of the conical intersection is lower than the one appearing in the curves. Some vibrational motions can therefore tend to displace

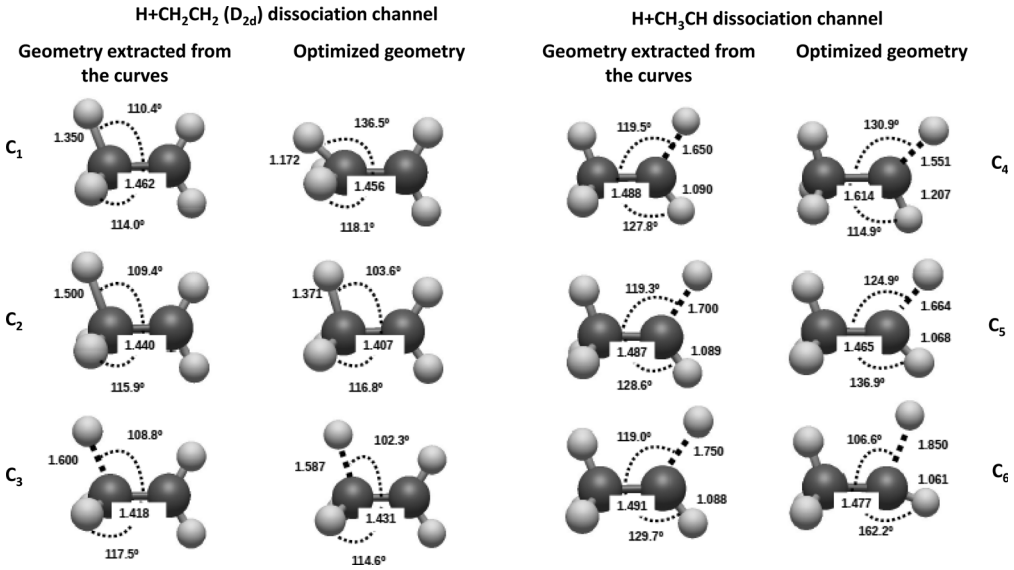

Fig. 7 Geometries of the conical intersection seams explored by the potential energy curves in comparison with the bottom of the seam optimized at an *ab initio* level. Left side: conical intersections corresponding to the H + CH_3CH dissociation channel represented in the bottom panel of Fig. 6. Right side: conical intersections corresponding to the H + CH_2CH_2 (D_{2d}) dissociation channel represented in the middle panel of Fig. 6.

the atoms so that the geometry is closer to the one characterizing the conical intersection seam. This particular vibrational mode will then favor the transition by helping to access a particular area of the potential energy surface where the conical intersection lies lower in energy.

As observed in Fig. 7, the geometries for the conical intersections labeled as C_1 to C_5 extracted from the curves are very similar to the corresponding optimized geometries. The conical intersection C_6, which plays a major role in the C_α site-specific mechanisms (*i.e.* channels **1b** and **2a**) (see Fig. 1 and 6), exhibits in contrast a significant change in the C–C–H angle. The rocking movement of the CH_2 moiety (C–C bending and twisting) can therefore allow meeting the tight geometry requirements and thus reaching the seam of this conical intersection. The rocking vibrational mode of the methylene group constitutes, therefore, a clear example of a promoting vibrational mode. Ethyl molecules with CH_2 rocking activity would proceed fast through the crossing with little or no time for IVR to occur. As a result, the C_α rocking vibration would be adiabatically preserved and inherited by the ethylidene CH_3CH fragment, which should show some internal rovibrational contents associated presumably with the C–C twisting and/or C_α-H stretching modes.

The site-specific mechanism $C_\beta H_3/C_\beta D_3$ associated with the twisted geometry of the ethyl radical (**2b**) constitutes, on the other hand, a typical case where the vibrational activity of the parent radical plays just a spectator role. The relevant conical intersection for the specific C_β-H dissociation is labeled as C_2 in Fig. 6 and 7. The only differing parameter between the *ab initio* and the C_2 geometries (Fig. 7) is the C_β-H stretching mode. The ethyl radical reaches, therefore, the conical intersection with the appropriate geometry and only a little adjustment of the C_β-H bond is needed. The C_β-H stretching mode acts as a spectator mode of the process. It should be noted that the spectator modes are adiabatically preserved during transfer through a conical intersection as well and, therefore, some related vibrational activities in the daughter radicals should appear.

We found that the behavior of the conical intersections is significantly affected by the isotopic effect. As mentioned before, the high-energy C_α site-specific mechanism (**2a**) is barely visible for the D-atom (Fig. 5d). In a standard fast dissociation process, the excited species are located in a region of the repulsive PES well above the asymptotic limit. The large translational energy content of the corresponding products follows the energy conservation law; *i.e.*, the initial potential energy is channeled into translational energy. In a case such as the high-energy C_α site-specific mechanism (**2a**), the ethyl radicals are excited at energies close to that of the asymptotic limit. In this particular situation, the translational energy content of the dissociating species allows overcoming the exit barrier (in the adiabatic representation) associated with the conical intersection. The larger momentum of inertia (heavier mass and lower velocity) of the D-atom plays here against the curve transfer, and only a little amount of the initially excited radicals proceed through the conical intersection.

Another interesting isotopic effect is observed when C_β (**2b**) in the CD_3CH_2 and CH_3CD_2 species is compared. The associated energy reference, indicated as a vertical bar, does not lie at the onset of the corresponding translational distribution for CD_3CH_2, as observed in Fig. 5(b). Such behavior indicates that an important part of the energy in excess of the excited ethyl radical is funneled into the internal degrees of freedom of the products. According to the discussion made, a couple of paragraphs above, there must exist some additional deviations from the conical intersection geometry, originated by the isotopic

substitution. If some rovibrational activities are induced in the ethylene product, the C_2 conical intersection must play an active role in the crossing, most probably associated with the presence of some vibrational promoting modes, and not with a geometry change imposed by the conical intersection, as the narrow width of the distribution suggests.

5. Conclusions

The site-specific photodissociation mechanism in the ethyl radical is interrogated through the velocity map imaging detection of H- and D-atoms produced in the C–H/C-D excision of *in situ* photolysis-generated CH_3CH_2, CD_3CD_2, CH_3CD_2, and CD_3CH_2 radicals. The results show that the internal energy requirement for the site-specific mechanism is not fulfilled at 201 nm for the C–D cleavage while at 193 nm, the available energy enables two additional site-specific reaction pathways associated with the $C_\alpha H_2$ and $C_\beta H_3$ moieties. The results are rationalized by means of high-level *ab initio* calculations of the potential energy surfaces and the corresponding non-adiabatic coupling matrix elements (NACMEs). Based on the relative intensities observed for the different dissociation channels and the associated width in the translational energy distributions, we discuss the play between the so-called vibrational promoting modes and the randomization of the internal energy among the different vibrational modes. Reaction dynamics calculations would be relevant in order to confirm the proposed mechanisms, although the large number of coupled electronic states and degrees of freedom make difficult to carry out such calculations in an accurate way.

Conflicts of interest

There are no conflicts to declare.

Acknowledgements

This research was carried out within the Unidad Asociada Química Física Molecular between the Departamento de Química Física of Universidad Complutense de Madrid and CSIC. D. V. C. acknowledges financial support from the Spanish MINECO under the FPI predoctoral program. This work was financed by the grants PGC2018-096444-B-I00, PID2019-107115GB-C21, PID2021-122839NB-I00, PID2021-122549NB-C21 and PID2021-122796NB-I00 from the MCIN/AEI/10.13039/501100011033/FEDER, UE. A. G. V. acknowledges support from the COST Action CA21101 (COSY). The facilities provided by the Centro de Láseres Ultrarrápidos at Universidad Complutense de Madrid are gratefully acknowledged. The Centro de Supercomputación de Galicia (CESGA, Spain) and the Centro Técnico de Informática (CTI, CSIC) are acknowledged for the use of their resources. This work was performed in part at the Institute of Electronic Structure and Laser, Foundation for Research and Technology-Hellas (IESL-FORTH) and received financial support from LaserLab Europe through the ULF-FORTH002262 project (Grant agreement no. 654148).

Notes and references

1 G. Balerdi, J. Woodhouse, A. Zanchet, R. de Nalda, M. L. Senent, A. García-Vela and L. Bañares, *Phys. Chem. Chem. Phys.*, 2016, **18**, 110.
2 S. Marggi Poullain, D. V. Chicharro, A. Zanchet, M. G. González, L. Rubio-Lago, M. L. Senent, A. García-Vela and L. Bañares, *Phys. Chem. Chem. Phys.*, 2016, **18**, 17054–17061.
3 A. Zanchet, L. Bañares, M. L. Senent and A. García-Vela, *Phys. Chem. Chem. Phys.*, 2016, **18**, 33195.
4 D. V. Chicharro, S. Marggi-Poullain, A. Zanchet, A. Bouallagui, A. García-Vela, M. L. Senent, L. Rubio-Lago and L. Bañares, *Chem. Sci.*, 2019, **10**, 6494–6502.
5 S. Marggi Poullain, D. V. Chicharro, A. Zanchet, L. Rubio-Lago, A. García-Vela and L. Bañares, *Phys. Chem. Chem. Phys.*, 2019, **21**, 23017–23025.
6 M. G. González, S. Marggi Poullain, L. Rubio-Lago and L. Bañares, *Phys. Chem. Chem. Phys.*, 2020, **22**, 5995.
7 D. V. Chicharro, A. Zanchet, A. Bouallagui, L. Rubio-Lago, A. García-Vela, L. Bañares and S. Marggi Poullain, *Phys. Chem. Chem. Phys.*, 2021, **23**, 2458–2468.
8 S. Marggi Poullain, L. Rubio-Lago, D. V. Chicharro, A. Boullagui, A. Zanchet, Y. Ounaies, A. García-Vela and L. Bañares, *Mol. Phys.*, 2022, **120**, e1984598.
9 J. L. Brum, S. Deshmukh and B. Koplitz, *J. Chem. Phys.*, 1990, **93**, 7504–7505.
10 J. L. Brum, S. Deshmukh and B. Koplitz, *J. Chem. Phys.*, 1991, **95**, 2200–2202.
11 J. L. Brum, S. Deshmukh, Z. Wang and B. Koplitz, *J. Chem. Phys.*, 1993, **98**, 1178–1192.
12 Z. Min, R. Quandt and R. Bersohn, *Chem. Phys. Lett.*, 1998, **296**, 372–376.
13 T. Gilbert, T. L. Grebner, I. Fischer and P. Chen, *J. Chem. Phys.*, 1999, **110**, 5485–5488.
14 G. Amaral, K. Xu and J. Zhang, *J. Chem. Phys.*, 2001, **114**, 5164–5169.
15 M. Steinbauer, J. Giegerich, K. H. Fischer and I. Fischer, *J. Chem. Phys.*, 2012, **137**, 014303.
16 J. M. Hostettler, A. Bach and P. Chen, *J. Chem. Phys.*, 2009, **130**, 034303.
17 A. F. Wagner, L. A. Rivera-Rivera, D. Bachellerie, J. W. Perry and D. L. Thompson, *J. Phys. Chem. A*, 2013, **117**, 11624–11639.
18 H. R. Wendt and H. E. Hunziker, *J. Chem. Phys.*, 1984, **81**, 717–723.
19 A. Zyubin, A. Mebel and S. Lin, *Chem. Phys. Lett.*, 2000, **323**, 441–447.
20 A. Matsugi, *J. Phys. Chem. Lett.*, 2013, **4**, 4237–4240.
21 S. M. Poullain, P. Recio, D. Chicharro, L. Rubio-Lago, J. González-Vázquez and L. Bañares, *Phys. Chem. Chem. Phys.*, 2019, **21**, 14250–14260.

22 L. Rubio-Lago, A. García-Vela, A. Arregui, G. A. Amaral and L. Bañares, *J. Chem. Phys.*, 2009, **131**, 174309.
23 H.-J. Werner, P. J. Knowles, G. Knizia, F. R. Manby, M. Schütz, P. Celani, T. Korona, R. Lindh, A. Mitrushenkov, G. Rauhut, K. R. Shamasundar, T. B. Adler, R. D. Amos, A. Bernhardsson, A. Berning, D. L. Cooper, M. J. O. Deegan, A. J. Dobbyn, F. Eckert, E. Goll, C. Hampel, A. Hesselmann, G. Hetzer, T. Hrenar, G. Jansen, C. Köppl, Y. Liu, A. W. Lloyd, R. A. Mata, A. J. May, S. J. McNicholas, W. Meyer, M. E. Mura, A. Nicklass, D. P. O'Neill, P. Palmieri, D. Peng, K. Pflüger, R. Pitzer, M. Reiher, T. Shiozaki, H. Stoll, A. J. Stone, R. Tarroni, T. Thorsteinsson and M. Wang, *MOLPRO, version 2015.1, a package of ab initio programs*, 2015.
24 V. Barone, *J. Chem. Phys.*, 2005, **122**, 014108.
25 M. J. Frisch, G. W. Trucks, H. B. Schlegel, G. E. Scuseria, M. A. Robb, J. R. Cheeseman, G. Scalmani, V. Barone, B. Mennucci and G. A. Petersson, *et al.*, *Gaussian 09, revision A 1*, Gaussian, 2010.
26 C. Moller and M. S. Plesset, *Phys. Rev.*, 1934, **46**, 0618–0622.
27 J. D. Rodríguez, M. G. González, L. Rubio-Lago, L. Bañares, P. C. Samartzis and T. N. Kitsopoulos, *J. Phys. Chem. A*, 2013, **117**, 8175–8183.
28 J. Muckerman, *J. Phys. Chem.*, 1989, **93**, 179–184.
29 V. Goncharov, N. Herath and A. G. Suits, *J. Phys. Chem. A*, 2008, **112**, 9423–9428.
30 S. Marggi Poullain, D. V. Chicharro, E. Navarro, L. Rubio-Lago, J. González-Vázquez and L. Bañares, *Phys. Chem. Chem. Phys.*, 2018, **20**, 3490–3503.

